Signatures of atomic structure in subfemtosecond laser-driven electron dynamics in nanogaps

Luke Bhan,[1] Cody Covington,[2] and Kálmán Varga[1,*]
[1]*Department of Physics and Astronomy, Vanderbilt University, Nashville, Tennessee 37235, USA*
[2]*Department of Chemistry, Austin Peay State University, Clarksville, Tennessee 37044, USA*

(Received 8 November 2021; accepted 8 February 2022; published 22 February 2022)

Coupled Maxwell and quantum-mechanical equations are used to simulate the electron dynamics in nanogaps in systems containing thousands of atoms. It will be shown that besides the carrier-envelop phase, bow-tie or gap shape, and gap size, the atomistic structure also significantly alters the electron dynamics. Atomic-scale interference fringes appear not only in the electron density but in the electron current and field enhancement as well. Electron bursts emerge from individual atoms and scatter on atoms driven by the direction of the laser. The time-dependent orbital-free density functional theory coupled to the Maxwell equations allows us to simulate physical systems approaching the realistic size and to explore the physical mechanism controlling the electron dynamics.

DOI: 10.1103/PhysRevB.105.085416

I. INTRODUCTION

The precise control of the carrier-envelope phase (CEP) of few-cycle laser pulses at subfemtosecond timescales allows the manipulation of electron dynamics by the electromagnetic field of light [1–7]. By suitable choice of the CEP, the oscillating electric field of a light wave can drive electrons across a nanoscale plasmonic gap several orders of magnitude faster than the gigahertz speed of conventional electronics [8–17]. Bow-tie antennas are particularly useful because they can significantly increase the electron emission by resonant plasmonic effects [4,15,18–24]. The excited plasmons can induce strong, localized electric fields, which can drive large electron currents from the nanostructures [19,25–30].

The electron transport between nanoparticles is controlled by several different factors. When the nanostructures are close to each other, their near fields couple to each other leading to enhancement depending on the distance, shape, and size of the nanoparticles [31]. The electron dynamics also depends on the energy of the photons as well as the duration and the CEP of the laser pulse.

To describe a realistic physical system, one needs to simulate thousands of atoms, which is very difficult for quantum-mechanical approaches. The time-dependent density functional theory (TDDFT) [32] is a method of choice, but TDDFT based calculations either use jellium models neglecting atomic details [33–36] or are restricted to small model systems [37–44].

The importance of the atomic structure [38,40] and the quantum effects [34] are well recognized and emphasized by the TDDFT calculations. For example, the individual atomic protrusions into the gap can significantly increase local electromagnetic enhancement in addition to the plasmonic fields [40,45] and quantum phenomena, such as confinement and tunneling play an important role [34].

Another important physical mechanism is the coupling between electromagnetic fields and matter. The electron current and time-dependent charge oscillations induce electric fields in a highly nonlinear manner. In TDDFT and other quantum-mechanical approaches this is usually neglected, while in electrodynamics simulation, the microscopic electron dynamics are not included.

In this work, we address both of these issues by coupling the atomistic quantum description of electron dynamics and the time-dependent electromagnetic fields to describe electron bursts and transport in plasmonic nanogaps. We show that, besides the carrier envelop phase, bow-tie or gap shape, and gap size, the atomistic structure also substantially changes the electron dynamics. In the simulations, atomic-scale interference fringes appear not only in the electron density but in the electron current and field enhancement as well. Electron bursts emerge from individual atoms and scatter on atoms driven by the direction of the laser. This interference and scattering modulate the electron dynamics on the atomic scale.

Both the coupling between light and matter and the atomistic description are very important in understanding the dynamics of ultrafast electron currents in nanogaps. To address these for realistic physical devices one has to be able to simulate the electron dynamics in systems with thousands of atoms. For small model systems the effect of coupling between light and matter is small because there are not enough charges to create large induced fields. The orbital-free (OF) density functional theory (DFT) [46] is a good approach for large systems because its main variable is the electron density and it computationally scales linearly with system size, and it has been used in million-atom material simulations [47]. We use the time-dependent DFT version of the OF-DFT, the OF-TDDFT, in our calculations. The OF-TDDFT is coupled with the Maxwell equations and the Maxwell equations are solved using the Riemann-Silbertsen vector to describe the

*kalman.varga@vanderbilt.edu

electromagnetic fields [48]. In a previous work we have shown that the currents and induced fields predicted by OF-TDDFT calculations are in very good agreement with TDDFT calculations for jellium sheets, jellium spheres, atomistic sheets, and icosahedron clusters [49].

II. FORMALISM

The OF-TDDFT equation is a time-dependent Schrödinger equation for a single orbital [49],

$$\left(i\hbar\frac{\partial}{\partial t} - H_{OF}\right)\Psi(\boldsymbol{r},t) = 0, \tag{1}$$

where

$$H_{OF}(\boldsymbol{r},t) = -\tfrac{1}{2m}[-i\hbar\nabla_{\boldsymbol{r}} - e\boldsymbol{A}(\boldsymbol{r},t)]^2 + V_{OF}[\rho](\boldsymbol{r},t). \tag{2}$$

The density-dependent potential V_{OF} is defined in Appendix A. The electron density and the electron current at time t are defined as

$$\rho_{OF}(\boldsymbol{r},t) = |\Psi(\boldsymbol{r},t)|^2 \tag{3}$$

and

$$\boldsymbol{J}_{OF}(\boldsymbol{r},t) = 2\mathrm{Re}\{\Psi(\boldsymbol{r},t)^*[-i\hbar\nabla_{\boldsymbol{r}} - e\boldsymbol{A}(\boldsymbol{r},t)]\Psi(\boldsymbol{r},t)\}. \tag{4}$$

To solve the Maxwell equations we use the Reimann-Silberstein (RS), which is coupled to the OF-TDDFT equation by the method developed in Ref. [48]. In this approach, the RS vector is defined as

$$\boldsymbol{F}(\boldsymbol{r},t) = \sqrt{\frac{\epsilon_0}{2}}\boldsymbol{E}(\boldsymbol{r},t) + i\sqrt{\frac{1}{2\mu_0}}\boldsymbol{B}(\boldsymbol{r},t), \tag{5}$$

and this vector satisfies the Maxwell equations in the form

$$i\hbar\frac{\partial \boldsymbol{F}}{\partial t} = c\left(\boldsymbol{S}\cdot\frac{\hbar}{i}\nabla_{\boldsymbol{r}}\right)\boldsymbol{F} - \frac{i\hbar}{\sqrt{2\epsilon_0}}\boldsymbol{J}, \tag{6}$$

where $\boldsymbol{S}$ is the spin-1 3×3 Pauli matrices. The main advantage of this approach is that Eq. (6) is similar to a time-dependent Schrödinger equation [Eq. (1)] and the RS vector can be calculated by time propagation together with the time-dependent wave function. The wave function is represented on a real-space grid and is time propagated using Taylor time evolution. The RS vector is represented and time propagated in Fourier space. A more detailed description can be found in Ref. [49]. In the numerical calculation, first, the ground state wave function is calculated by diagonalizing H_{OF} on a real space grid, and this will be used as the initial wave function. An external laser pulse is added to the system of the form

$$E_z(\boldsymbol{r},t) = E_0\sin[\omega(t - x/c) + \phi]e^{-(t-t_0-x/c)^2/\alpha^2}\Gamma(t), \tag{7}$$

where $\Gamma(t)$ is a ramping function that ensures the electric field is zero at $t = 0$, α is the carrier-envelope width, ω is the field frequency, E_0 is the field strength, and ϕ is the carrier-envelope phase. The parameters of the laser pulse and the pulse shape for different carrier-envelope phases and other details of the numerical solution of the coupled equations are shown in Appendix A. Atomic units are used in the calculations and the conversion factors to electron volts and femtoseconds are given in Appendix A.

III. RESULTS

We use aluminum bow-tie structures similar to the one in Fig. 1 to study the electron dynamics in nanogaps. The two main variables of this geometry are the distance between the tips and the bow-tie angle (see Appendix A). Aluminum bow-tie structures are considered good alternatives [50–52] to noble metal (gold and silver) bow-tie structures, and their field enhancement properties have been investigated experimentally [22,51,53,54] and by finite-difference time-domain simulations [55–58]. The field enhancement in the gap is found to be between 20 and 100 [55,56,58] depending on the geometry of the structure. This is somewhat smaller than the field enhancement in gold bow-tie antennas [4,20].

In the simulations, the electric field from the laser drives the electron density to the tips of the bow-tie structure, creating a strong induced electric field around the tip. Snapshots of the electron density, the electron current, and the electric field are shown in Fig. 1 for $\phi = 0$. In these figures (6000 atoms and 18 000 electrons are used in this example), the fingerprint of the underlying atomic structure can clearly be seen in the density, the current, and the electric field. The electron current is emitted not only from the tip atoms but also from a wider region and the absorption extends into layers of atoms. This is even more visible in the excited state density $[\rho(t) - \rho(0)]$ where the charge density on individual atoms deep inside the tips varies with the electric field [see Fig. 1(c)]. The snapshots in Fig. 1(c) demonstrate that the electron transport and dynamics evolve through excitation of individual atoms.

The induced electric field [Fig. 1(d)] and the electron current [Fig. 1(e)] also change on the atomic scale in space. Figure 1(d) shows that the electric field is strong inside the tips and interferencelike fringes commensurate with the atomic structure are present. The figures also show that the electric fields and currents change signs between atoms or atomic layers, corroborating that the atomic structure is important and strongly influences the electron dynamics.

Figure 1(f) shows the field enhancement at a frequency of $\omega = 0.16$, where the enhancement is the largest. The bright spots correspond to an enhancement of a factor of 40–45. There is a bright hot spot along the line that connects the two tips and reaches inside the tip region deep inside the atomic layers where two small hot spots can also be seen.

To analyze the flow of electrons from one tip to another, the flux of electrons through a given surface are calculated as

$$\Phi(t) = -\int dxdyJ_z(\boldsymbol{r},t), \quad \Phi_T = \int_0^T dt\,\Phi(t). \tag{8}$$

Figure 2(a) shows the flux of electrons between the tips. The surface is taken to be the xy plane which lies in between the two structures. When the laser field is symmetric ($\phi = 0$), it moves the electrons from one tip to the other and back, leading to a net transfer across the bow-tie structure of close to 0. The amplitude of the laser field reaches its first maxima at around $t = 30$ a.u. and reaches the second one, with the opposite sign, at $t = 45$ a.u. The flux follows this oscillation with a 20-a.u. time delay. The figure also shows the importance of coupling the Maxwell and OF-TDDFT equations. In the uncoupled case, the induced fields due to the dynamics of electrons are neglected and the flux is about two times bigger than in the

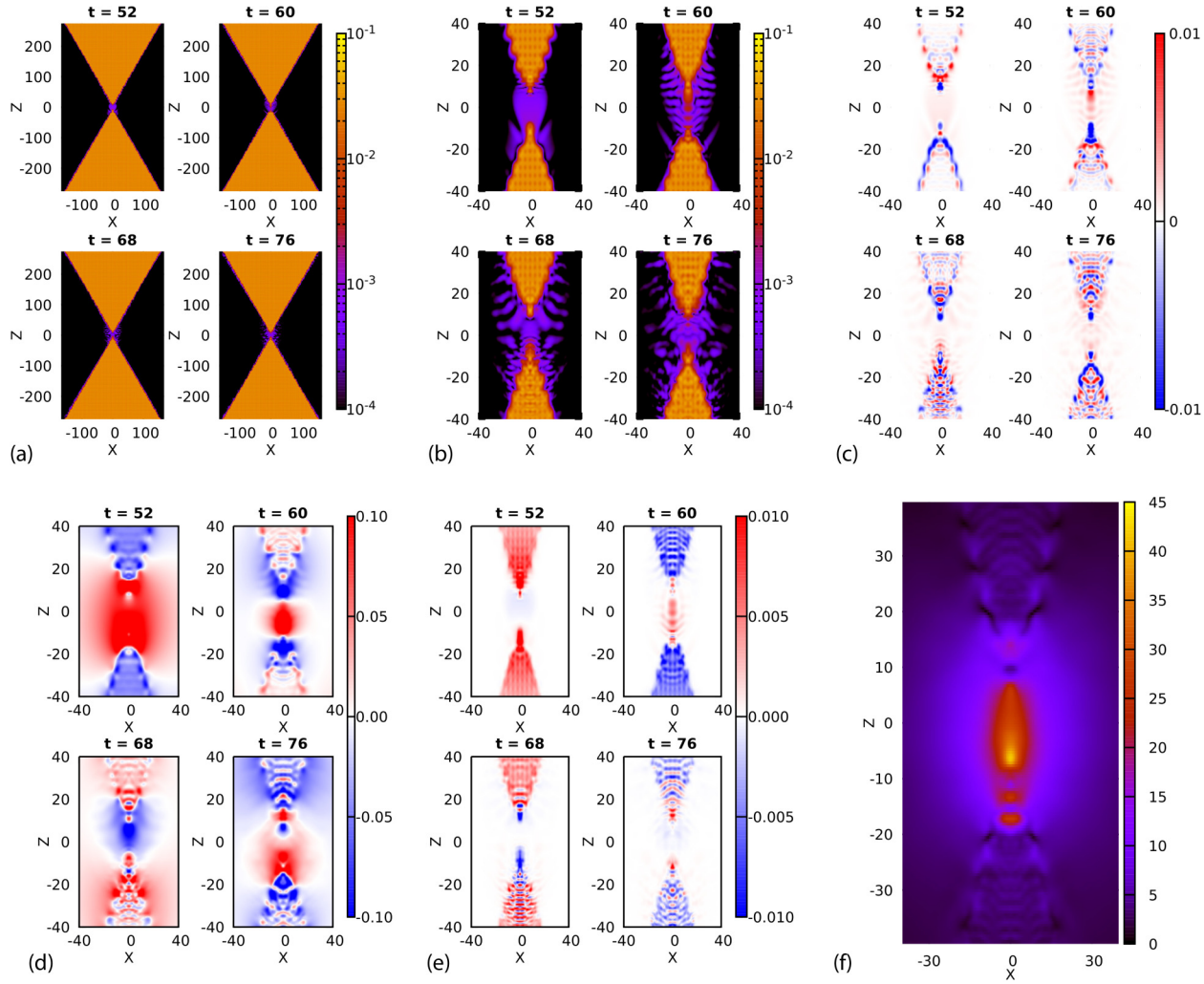

FIG. 1. Electron density (a), electron density in the gap region (b), excited-state electron density, $\rho(t) - \rho(0)$, in the gap region (c), electric field in the gap (d), current in the gap (e), and field enhancement in the gap (f) in a bow-tie structure. The figures were obtained by averaging over the y direction. Six thousand atoms with 18 000 electrons were used.

coupled case. We also considered the effect of system size on the flux. Figure 2 shows that the time dependence of the flux for a smaller system is very similar to that of the larger system, but the flux transfer is somewhat smaller.

The number of transported electrons from one tip to the other strongly depends on the CEP. Figure 2(b) shows the flux for different ϕ values between 0 and 2π. CEP values of $\phi = \pi/2$ and $\phi = 3\pi/2$ have the largest net electron transport, and they move the electrons in the opposite directions, as dictated by the symmetry of the laser. In this case, the maximum transfer is 0.5 electrons over a time frame of 70 a.u., corresponding to a current of 50 μA which is very large. The field enhancement [see Fig. 2(c)] seems to have a very small dependence on the CEP.

Next, we study the effect of gap size on the electron transport between the tips. In these simulations, the distance between the tips is varied and the same laser is used as before with a CEP of $\phi = 0$. The gap size is defined as the distance between the outermost atoms on the tips. As expected, with a larger gap size, there is a smaller induced field amplitude and thus a smaller field enhancement [Fig. 2(e)]. In particular, for approximately every 2 a.u. (0.1 nm) increase in gap size, there is a 10% drop in the overall enhancement.

Figure 2(f) shows that the net electron transport between the tips strongly depends on the gap distance. This is because the large gap size inhibits the electrons from moving back when the laser changes direction because there is a time delay in the transport process. The larger the gap, the farther the electrons have to travel, meaning the electron packet does not make it across the gap before the laser field reverses. This example shows that one can use the gap size to control the electron transfer between tips.

The appeal of the bow-tie system with a single pulsed asymmetric laser is that electron transport can occur without a bias. However, it is still worth exploring the amplification of transport by a bias as it is commonly used in chip technologies. These calculations use the same laser as before, but a bias potential is added with a voltage that is equal to a certain percentage of the maximum laser amplitude, E_0, for the entire duration of the simulation. We utilize bias voltage values of 0.016 (8.39 V/nm), 0.032 (16.78 V/nm), 0.049 (25.16 V/nm), 0.065 (33.56 V/nm), and 0.082 (41.95 V/nm);

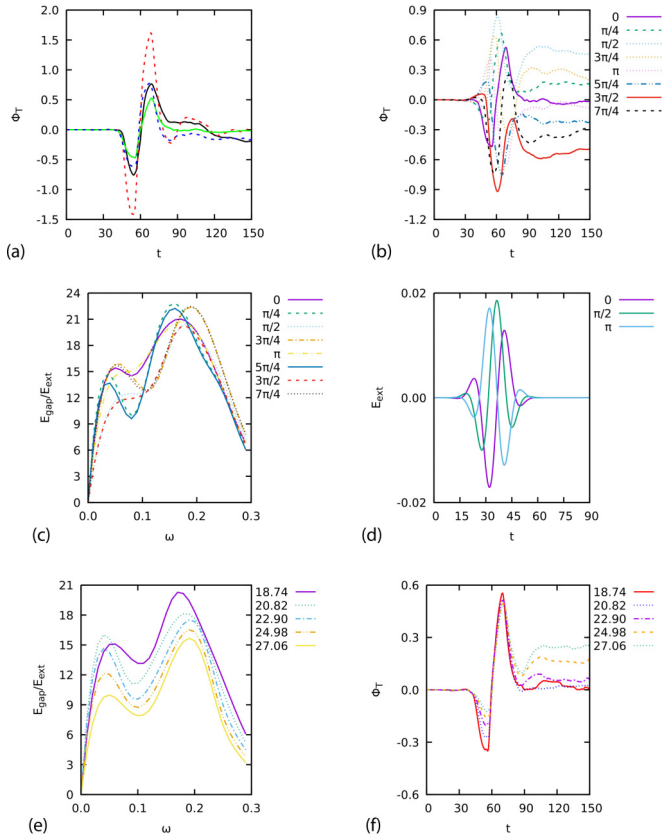

FIG. 2. Fluxes and field enhancements for various carrier-envelope phases. (a) Fluxes in two systems of different sizes (small and medium) are compared. The parameters defining the systems are listed in Appendix A. The dashed red line is the flux without coupling and the solid black line is the flux with coupling in the medium-sized system. The dashed blue line is the flux withoutcoupling and the solid green line is the flux with coupling in the small system. (b) Fluxes for different carrier-envelope phases. (c) Field enhancements for different carrier-envelope phases. (d) Laser field for different CEPs. (e) Enhancement and (f) flux for different gap sizes. The frequency and time are in atomic units, and the flux is the number of electrons crossing the surface in the gap.

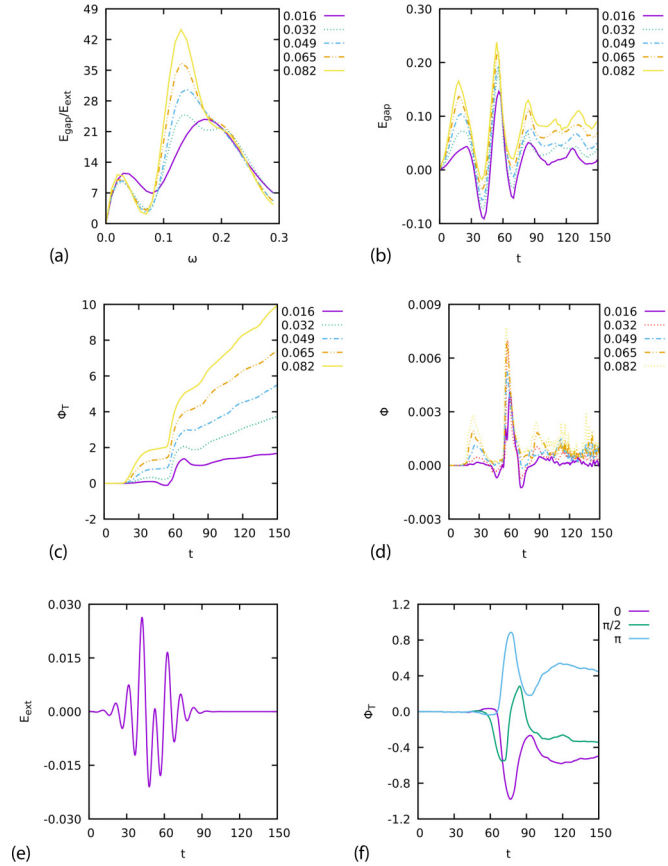

FIG. 3. Field enhancement (a), electric field (b), flux (c), and flux at time t (d) for a biased laser pulse. Laser (e) and flux of multiple CEPs (f) for two-colored laser pulses. The frequency and time are in atomic units, and the flux is the number of electrons crossing the surface in the gap.

ranging between 10 and 50% of E_0. The larger the bias, the larger the field amplitude; however, there is a new oscillation when compared to a nonbiased field at time $t = 15$ to $t = 30$, shown in Fig. 3(b). In the nonbiased case [Fig. 2(a)], there is no flux before $t = 30$ and the new peak is due to the bias. Figure 3(a) shows that the bias significantly increases the field enhancement. This is the consequence of the increased electron current in the gap region [Fig. 3(a)], especially for large biases. Additionally, the electron transfer, shown in Fig. 3(c), continues in the direction of the bias as long as the bias stays active even after the laser pulse. As expected, these fluxes are much larger than those in the nonbiased case. Figure 3(d) shows the flux as the function of time. One can see that flux is driven by the electric field [see Figs. 3(b) and 3(c)], but there is a time delay between the two.

In the following, we explore another possibility to asymmetrically transfer electrons across the gap using a multicolor laser [shown in Fig. 3(e)]. A combination of two wavelengths of frequencies of ω and 2ω is used to create this pulse (for definition, see Appendix A). Fig. 3(f) shows that the field flux is still similar to the single-color pulse laser despite reaching a much higher laser amplitude [almost 0.27 a.u. as shown in Fig. 3(e) compared to 0.19 in the case of the single pulse]. The biggest effect of the two-color laser is that it changes the CEP dependence of the flux. The largest flux is at $\phi = 0$ and $\phi = \pi$, while the single pulsed laser had the largest flux at $\phi = \frac{\pi}{2}$. The most interesting effect of the multicolor laser is that it can be used to change the direction of the electron current. For example, using $\phi = \frac{\pi}{2}$ with a single color laser the net electron flow is from the upper tip to the lower tip [Fig. 2(b)]. By turning on the second laser [Fig. 3(f)] the electrons will flow in the opposite direction. Further details of the multicolor case are highlighted in Appendix B.

Finally, we have also investigated bow-tie structures with asymmetric tips (see Fig. 4). Asymmetric structures can create net electron transport between the tips for all values of the CEP. Several different geometries were investigated. In asymmetric sharp-blunt bow-tie structures, the field enhancement does not significantly change (Fig. 4), but using different shapes, one can steer the current from the sharper tip to the wider tip even with $\phi = 0$. The field enhancement around a

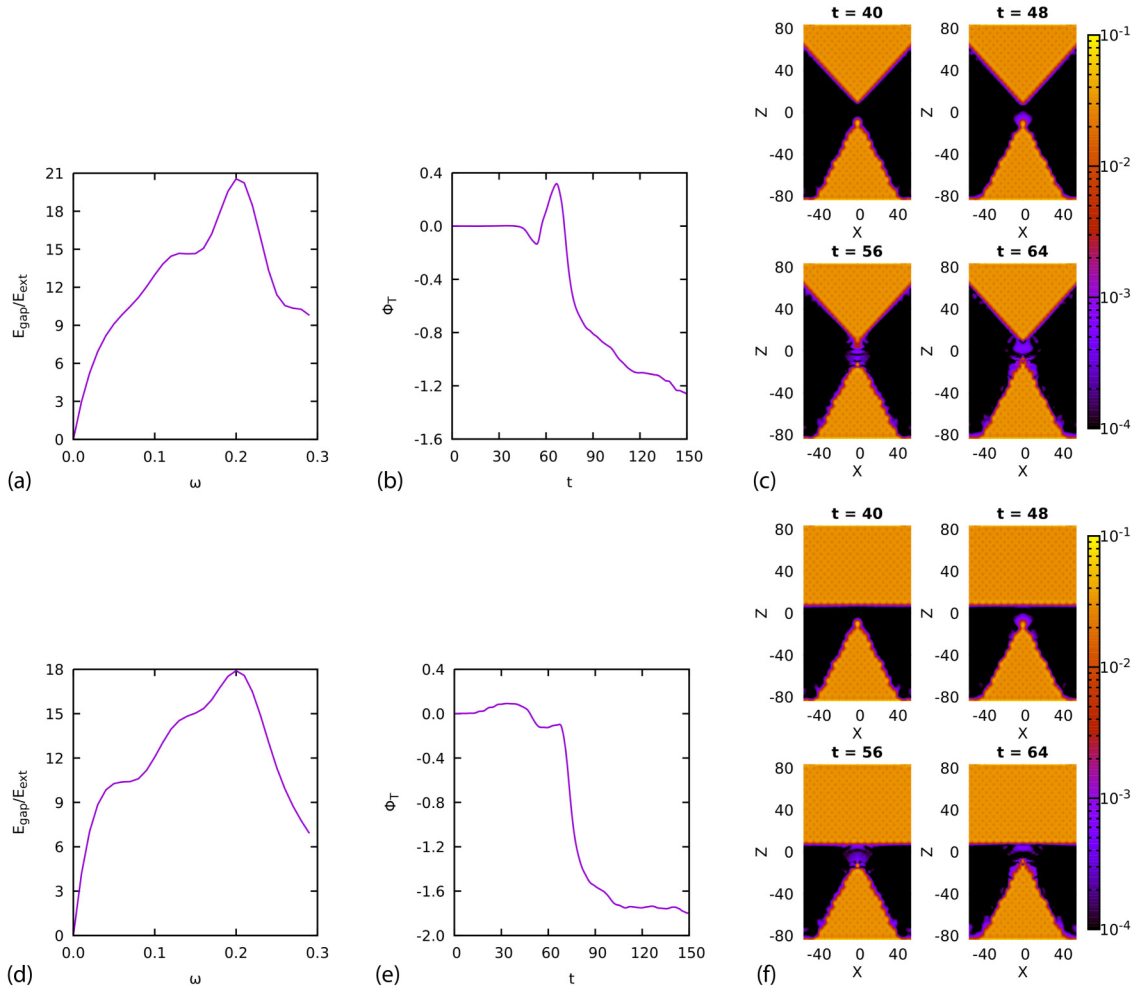

FIG. 4. Field enhancement [panels (a) and (d)], flux [panels (b) and (e)], and density snapshots [panels (c) and (f)] in asymmetric bow-tie structures. The CEP is $\phi = 0$. The frequency and time are in atomic units and the flux is the number of electrons crossing the surface in the gap.

single tip (without the other tip) is about $1/3$ of the field enhancement of the asymmetric structures, so even a flat surface increases the field enhancement in the gap. Figure 4 shows that the current now flows in one direction outward from the tip. This geometry allows sending electron packets from the sharp tip to a wider tip or to a sheet controlled by the laser without relying on the CEP.

IV. SUMMARY

In summary, coupled OF-TDDFT Maxwell simulations have been performed on aluminum bow-tie systems comprised of thousands of atoms. Atomistic features appear in the time-dependent electron densities, currents, and induced electric fields, indicating the importance of the atomistic description. These OF-TDDFT calculations substantially extend the applicability of quantum-mechanical simulations and the atomistic simulation of realistic devices are within the reach of this approach. We have shown that unidirectional currents can be generated in several different ways, e.g., with optimized CEPs, with multicolor lasers, or by using asymmetric bow-tie structures. These atomistic coupled OF-TDDFT Maxwell simulations might be useful in the investigation of various nanoscale devices where the interaction of electromagnetic fields and matter is important.

APPENDIX A: COMPUTATIONAL DETAILS

In our calculations we define the orbital-free potential as

$$V_{OF}(\boldsymbol{r},t) = V_{\text{ext}}(\boldsymbol{r}) + V_{xc}(\boldsymbol{r}) + V_H(\boldsymbol{r}) + V_{TF}[\rho](\boldsymbol{r}) + V_W[\rho](\boldsymbol{r}), \tag{A1}$$

where V_{ext} is the potential induced from the external laser, V_{xc} is the exchange-correlation potential, V_H is the Hartree potential, V_{TF} is the Thomas-Fermi kinetic energy functional, and V_W is the von Weizsäcker potential. The OF-TDDFT and Maxwell equations are solved by time propagation [48]. The time propagation starts from a converged ground-state wave function using a 0.02-a.u time step for the wave function and a 0.001-a.u. time step for propagation of the electromagnetic (EM) fields in the coupled case. The Helmholtz decomposition of the Riemann-Silberstein vector allows the removal of the longitudinal component and then the Hartree potential can be calculated by solving the Poisson equation. The electron density and current are calculated by the TD-OFDFT equation and then used to calculated $\boldsymbol{F}$ at time $t + \Delta t/2$ by

TABLE I. A table describing all the system sizes and parameters used in our simulations. The grid spacing and time steps are in atomic units. (EM is already defined) The time step used in the quantum mechanical part (QM) and in the EM part are denoted by $dt(QM)$ and $dt(EM)$, respectively.

System	Angle	Gap size	Number of atoms	Grid size	Grid spacing	dt (QM)	dt (EM)
Large standard	60	16.66	5660	$702 \times 16 \times 1152$	0.477 87	0.02	0.001
Medium standard	60	16.66	1848	$450 \times 16 \times 672$	0.477 87	0.02	0.001
Small standard	60	16.66	464	$237 \times 16 \times 352$	0.477 87	0.02	0.001
Small gap 1	60	18.74	464	$237 \times 16 \times 356$	0.477 87	0.02	0.001
Small gap 2	60	20.82	464	$237 \times 16 \times 360$	0.477 87	0.02	0.001
Small gap 3	60	22.90	464	$237 \times 16 \times 364$	0.477 87	0.02	0.001
Small gap 4	60	24.98	464	$237 \times 16 \times 368$	0.477 87	0.02	0.001
Small gap 5	60	27.06	464	$237 \times 16 \times 372$	0.477 87	0.02	0.001
Small angle 1	45	16.66	800	$384 \times 16 \times 352$	0.477 87	0.02	0.001
Small angle 2	30	16.66	1136	$384 \times 16 \times 352$	0.477 87	0.02	0.001
Small angle 3	15	16.66	1136	$384 \times 16 \times 352$	0.477 87	0.02	0.001

time propagating the Maxwell equation. Once $\boldsymbol{F}$ is known, $\boldsymbol{A}$ is calculated from the field $\boldsymbol{E}$ using the leapfrog algorithm described in Ref. [48].

The external laser pulse used in the calculations is defined as

$$\boldsymbol{E}_{\text{ext}}(\boldsymbol{r}, t) = (0, 0, E_0 \sin[\omega(t - x/c) + \phi]e^{-(t-t_0-x/c)^2/\alpha^2}), \tag{A2}$$

where α is the envelope width, ω is the frequency, and ϕ is the carrier-envelope phase. The laser parameters are $E_0 = 0.019$, $\omega = 0.3$, and $\alpha = 10$ in atomic units. In atomic units $E_0 = 1$ a.u. corresponds to 51.422 V/Å, $\omega = 1$ a.u. is 45.6 nm, and 1 a.u. of time is 0.024 188 fs. Figure 3(e) shows an example of our short asymmetric laser with these parameters.

The field enhancements are calculated using

$$\text{Field Enhancement } (\boldsymbol{r}, \omega) = \boldsymbol{E}(\boldsymbol{r}, \omega)/\boldsymbol{E}_{\text{ext}}(\boldsymbol{r}, \omega). \tag{A3}$$

Here the ratio is taken in frequency space since the induced field is often quite different from the external field as a function of time.

We use bow-tie systems of Al atoms in the calculations. The largest system has 6000 atoms and 18 000 electrons. The bow-tie system in Fig. 5 ($\theta = \pi/3$) has 1848 atoms and 5544 electrons in a $215 \times 7.65 \times 321$ box with 0.478 grid spacing (all in atomic units) and periodic boundary conditions. We have also used a smaller structure (464 atoms and 1392 electrons) with the same angle and several other bow-tie systems with different angles. These systems produced results similar to those of the large system but required much less computational time. The details of the test system geometries are given in Table I.

For the asymmetric laser calculations, we have used the following multiwavelength laser:

$$E_{\text{multi}} = E_{\text{ext}}(\boldsymbol{r}, t, \omega = 0.3, \alpha = 10, E_0 = 0.019, \phi = 0) + E_{\text{ext}}(\boldsymbol{r}, t, \omega = 0.6, \alpha = 10, E_0 = 0.019, \phi = 0). \tag{A4}$$

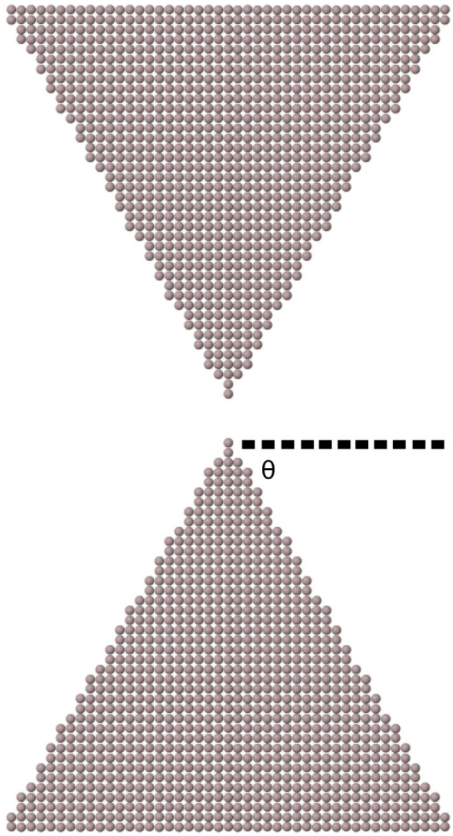

FIG. 5. Bow-tie structure.

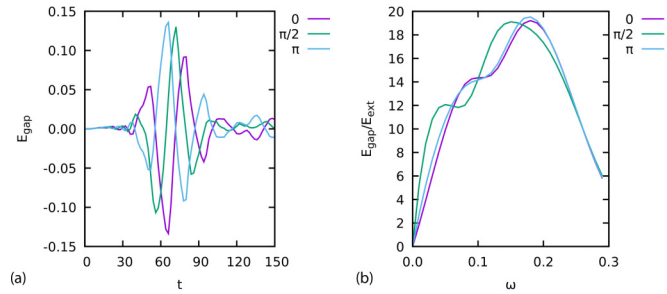

FIG. 6. Electric field (a) and field enhancement (b) of multicolored laser. The frequency and time are in atomic units.

APPENDIX B: FIELD ENHANCEMENT FOR MULTICOLORED LASER

For the multicolored laser we have omitted the field and the field enhancement in the main part of the paper as they are similar to that of a single-colored laser. We include them here in Fig. 6 for completeness. The figures show that, while the flux is very different from that of the single-color case [as shown in Fig. 2(b) and Fig. 3(f)] the field enhancement is similar to that of the single-color case.

[1] M. Hentschel, R. Kienberger, C. Spielmann, G. A. Reider, N. Milosevic, T. Brabec, P. Corkum, U. Heinzmann, M. Drescher, and F. Krausz, Attosecond metrology, Nature (London) **414**, 509 (2001).

[2] E. Goulielmakis, V. S. Yakovlev, A. L. Cavalieri, M. Uiberacker, V. Pervak, A. Apolonski, R. Kienberger, U. Kleineberg, and F. Krausz, Attosecond control and measurement: Lightwave electronics, Science **317**, 769 (2007).

[3] F. Krausz and M. Ivanov, Attosecond physics, Rev. Mod. Phys. **81**, 163 (2009).

[4] P. Dombi, Z. Pápa, J. Vogelsang, S. V. Yalunin, M. Sivis, G. Herink, S. Schäfer, P. Groß, C. Ropers, and C. Lienau, Strong-field nano-optics, Rev. Mod. Phys. **92**, 025003 (2020).

[5] M. Krüger, C. Lemell, G. Wachter, J. Burgdörfer, and P. Hommelhoff, Attosecond physics phenomena at nanometric tips, J. Phys. B: At., Mol. Opt. Phys. **51**, 172001 (2018).

[6] J. J. Baumberg, J. Aizpurua, M. H. Mikkelsen, and D. R. Smith, Extreme nanophotonics from ultrathin metallic gaps, Nat. Mater. **18**, 668 (2019).

[7] J. Lee, D.-J. Jeon, and J.-S. Yeo, Quantum plasmonics: Energy transport through plasmonic gap, Adv. Mater. **33**, 2006606 (2021).

[8] M. Ludwig, G. Aguirregabiria, F. Ritzkowsky, T. Rybka, D. C. Marinica, J. Aizpurua, A. G. Borisov, A. Leitenstorfer, and D. Brida, Sub-femtosecond electron transport in a nanoscale gap, Nat. Phys. **16**, 341 (2020).

[9] L. Shi, I. Babushkin, A. Husakou, O. Melchert, B. Frank, J. Yi, G. Wetzel, A. Demircan, C. Lienau, H. Giessen, M. Ivanov, U. Morgner, and M. Kovacev, Femtosecond field-driven on-chip unidirectional electronic currents in nonadiabatic tunneling regime, Laser Photonics Rev. **15**, 2000475 (2021).

[10] M. Ludwig, A. K. Kazansky, G. Aguirregabiria, D. C. Marinica, M. Falk, A. Leitenstorfer, D. Brida, J. Aizpurua, and A. G. Borisov, Active control of ultrafast electron dynamics in plasmonic gaps using an applied bias, Phys. Rev. B **101**, 241412(R) (2020).

[11] D. Buckley, Y. Yang, Y. Yang-Keathley, K. K. Berggren, and P. D. Keathley, Nanoantenna design for enhanced carrier–envelope-phase sensitivity, J. Opt. Soc. Am. B **38**, C11 (2021).

[12] Y. Yang, M. Turchetti, P. Vasireddy, W. P. Putnam, O. Karnbach, A. Nardi, F. X. Kärtner, K. K. Berggren, and P. D. Keathley, Light phase detection with on-chip petahertz electronic networks, Nat. Commun. **11**, 3407 (2020).

[13] M. R. Bionta, F. Ritzkowsky, M. Turchetti, Y. Yang, D. Cattozzo Mor, W. P. Putnam, F. X. Kärtner, K. K. Berggren, and P. D. Keathley, On-chip sampling of optical fields with attosecond resolution, Nat. Photonics **15**, 456 (2021).

[14] M. Turchetti, M. R. Bionta, Y. Yang, F. Ritzkowsky, D. R. Candido, M. E. Flatté, K. K. Berggren, and P. D. Keathley, Impact of DC bias on weak optical-field-driven electron emission in nano-vacuum-gap detectors, J. Opt. Soc. Am. B **38**, 1009 (2021).

[15] T. Rybka, M. Ludwig, M. F. Schmalz, V. Knittel, D. Brida, and A. Leitenstorfer, Sub-cycle optical phase control of nanotunnelling in the single-electron regime, Nat. Photonics **10**, 667 (2016).

[16] C. Karnetzky, P. Zimmermann, C. Trummer, C. Duque Sierra, M. Wörle, R. Kienberger, and A. Holleitner, Towards femtosecond on-chip electronics based on plasmonic hot electron nano-emitters, Nat. Commun. **9**, 2471 (2018).

[17] G. M. Rossi, R. E. Mainz, Y. Yang, F. Scheiba, M. A. Silva-Toledo, S.-H. Chia, P. D. Keathley, S. Fang, O. D. Mücke, C. Manzoni, G. Cerullo, G. Cirmi, and F. X. Kärtner, Sub-cycle millijoule-level parametric waveform synthesizer for attosecond science, Nat. Photonics **14**, 629 (2020).

[18] W. P. Putnam, R. G. Hobbs, P. D. Keathley, K. K. Berggren, and F. X. Kärtner, Optical-field-controlled photoemission from plasmonic nanoparticles, Nat. Phys. **13**, 335 (2017).

[19] R. G. Hobbs, W. P. Putnam, A. Fallahi, Y. Yang, F. X. Kärtner, and K. K. Berggren, Mapping photoemission and hot-electron emission from plasmonic nanoantennas, Nano Lett. **17**, 6069 (2017).

[20] P. J. Schuck, D. P. Fromm, A. Sundaramurthy, G. S. Kino, and W. E. Moerner, Improving the Mismatch between Light and Nanoscale Objects with Gold Bowtie Nanoantennas, Phys. Rev. Lett. **94**, 017402 (2005).

[21] M. Parzefall and L. Novotny, Optical antennas driven by quantum tunneling: A key issues review, Rep. Prog. Phys. **82**, 112401 (2019).

[22] B. Cerjan, X. Yang, P. Nordlander, and N. J. Halas, Asymmetric aluminum antennas for self-calibrating surface-enhanced infrared absorption spectroscopy, ACS Photonics **3**, 354 (2016).

[23] M. Runge, D. Engel, M. Schneider, K. Reimann, M. Woerner, and T. Elsaesser, Spatial distribution of electric-field enhancement across the gap of terahertz bow-tie antennas, Opt. Express **28**, 24389 (2020).

[24] A. Bhattacharya, G. Georgiou, S. Sawallich, C. Matheisen, M. Nagel, and J. Gómez Rivas, Large near-to-far field spectral shifts for terahertz resonances, Phys. Rev. B **93**, 035438 (2016).

[25] P. Dombi, A. Hörl, P. Rácz, I. Márton, A. Trügler, J. R. Krenn, and U. Hohenester, Ultrafast strong-field photoemission from plasmonic nanoparticles, Nano Lett. **13**, 674 (2013).

[26] H. Robatjazi, S. Bahauddin, C. Doiron, and I. Thomann, Direct plasmon-driven photoelectrocatalysis, Nano Lett. **15**, 6155 (2015).

[27] C. M. Scheffler, R. C. Word, and R. Könenkamp, Controlling electric field and photoemission at the tips of triangular gold antennas, Plasmonics **16**, 371 (2021).

[28] Y. Shen, H. Chen, N. Xu, Y. Xing, H. Wang, R. Zhan, L. Gong, J. Wen, C. Zhuang, X. Chen, X. Wang, Y. Zhang, F. Liu, J. Chen, J. She, and S. Deng, A plasmon-mediated electron emission process, ACS Nano **13**, 1977 (2019).

[29] P. Zimmermann, A. Hötger, N. Fernandez, A. Nolinder, K. Müller, J. J. Finley, and A. W. Holleitner, Toward plasmonic tunnel gaps for nanoscale photoemission currents by on-chip laser ablation, Nano Lett. **19**, 1172 (2019).

[30] K. Takano, M. Asai, K. Kato, H. Komiyama, A. Yamaguchi, T. Iyoda, Y. Tadokoro, M. Nakajima, and M. I. Bakunov, Terahertz emission from gold nanorods irradiated by ultrashort laser pulses of different wavelengths, Sci. Rep. **9**, 3280 (2019).

[31] J. Heimerl, T. Higuchi, M. Ammon, M. A. Schneider, and P. Hommelhoff, Gap-size dependence of optical near fields in a variable nanoscale two-tip junction, Phys. Rev. B **101**, 125403 (2020).

[32] E. Runge and E. K. U. Gross, Density-Functional Theory for Time-Dependent Systems, Phys. Rev. Lett. **52**, 997 (1984).

[33] D. C. Marinica, A. K. Kazansky, P. Nordlander, J. Aizpurua, and A. G. Borisov, Quantum plasmonics: Nonlinear effects in the field enhancement of a plasmonic nanoparticle dimer, Nano Lett. **12**, 1333 (2012).

[34] W. Zhu, R. Esteban, A. G. Borisov, J. J. Baumberg, P. Nordlander, H. J. Lezec, J. Aizpurua, and K. B. Crozier, Quantum mechanical effects in plasmonic structures with subnanometre gaps, Nat. Commun. **7**, 11495 (2016).

[35] G. Aguirregabiria, D.-C. Marinica, M. Ludwig, D. Brida, A. Leitenstorfer, J. Aizpurua, and A. G. Borisov, Dynamics of electron-emission currents in plasmonic gaps induced by strong fields, Faraday Discuss. **214**, 147 (2019).

[36] T. V. Teperik, P. Nordlander, J. Aizpurua, and A. G. Borisov, Robust Subnanometric Plasmon Ruler by Rescaling of the Nonlocal Optical Response, Phys. Rev. Lett. **110**, 263901 (2013).

[37] K. Uchida and K. Watanabe, Plasmon excitation and electron emission of a carbon nanotube under a linearly polarized laser: A real-time first-principles study, Phys. Rev. B **96**, 125419 (2017).

[38] P. Zhang, J. Feist, A. Rubio, P. García-González, and F. J. García-Vidal, *Ab initio* nanoplasmonics: The impact of atomic structure, Phys. Rev. B **90**, 161407(R) (2014).

[39] A. Varas, P. García-González, F. J. García-Vidal, and A. Rubio, Anisotropy effects on the plasmonic response of nanoparticle dimers, J. Phys. Chem. Lett. **6**, 1891 (2015).

[40] M. Barbry, P. Koval, F. Marchesin, R. Esteban, A. G. Borisov, J. Aizpurua, and D. Sánchez-Portal, Atomistic near-field nanoplasmonics: Reaching atomic-scale resolution in nanooptics, Nano Lett. **15**, 3410 (2015).

[41] R. Jestädt, M. Ruggenthaler, M. J. T. Oliveira, A. Rubio, and H. Appel, Light-matter interactions within the Ehrenfest-Maxwell-Pauli-Kohn-Sham framework: Fundamentals, implementation, and nano-optical applications, Adv. Phys. **68**, 225 (2019).

[42] M. Kuisma, A. Sakko, T. P. Rossi, A. H. Larsen, J. Enkovaara, L. Lehtovaara, and T. T. Rantala, Localized surface plasmon resonance in silver nanoparticles: Atomistic first-principles time-dependent density-functional theory calculations, Phys. Rev. B **91**, 115431 (2015).

[43] E. Makkonen, T. P. Rossi, A. H. Larsen, O. Lopez-Acevedo, P. Rinke, M. Kuisma, and X. Chen, Real-time time-dependent density functional theory implementation of electronic circular dichroism applied to nanoscale metal-organic clusters, J. Chem. Phys. **154**, 114102 (2021).

[44] G. Giannone and F. Della Sala, Minimal auxiliary basis set for time-dependent density functional theory and comparison with tight-binding approximations: Application to silver nanoparticles, J. Chem. Phys. **153**, 084110 (2020).

[45] F. Marchesin, P. Koval, M. Barbry, J. Aizpurua, and D. Sánchez-Portal, Plasmonic response of metallic nanojunctions driven by single atom motion: Quantum transport revealed in optics, ACS Photonics **3**, 269 (2016).

[46] W. C. Witt, B. G. del Rio, J. M. Dieterich, and E. A. Carter, Orbital-free density functional theory for materials research, J. Mater. Res. **33**, 777 (2018).

[47] L. Hung and E. A. Carter, Accurate simulations of metals at the mesoscale: Explicit treatment of 1 million atoms with quantum mechanics, Chem. Phys. Lett. **475**, 163 (2009).

[48] C. Covington, D. Kidd, H. Buckner, H. Appel, and K. Varga, Time propagation of the coupled Maxwell and Kohn-Sham equations using the Riemann-Silberstein formalism, Phys. Rev. E **100**, 053301 (2019).

[49] C. Covington, J. Malave, and K. Varga, Coupled Maxwell and time-dependent orbital-free density functional calculations, Phys. Rev. B **103**, 075119 (2021).

[50] M. W. Knight, N. S. King, L. Liu, H. O. Everitt, P. Nordlander, and N. J. Halas, Aluminum for plasmonics, ACS Nano **8**, 834 (2014).

[51] S. Ambardar, D. Nguyen, G. Binder, Z. W. Withers, and D. V. Voronine, Quantum leap from gold and silver to aluminum nanoplasmonics for enhanced biomedical applications, Appl. Sci. **10**, 4210 (2020).

[52] D. Gérard and S. K. Gray, Aluminium plasmonics, J. Phys. D **48**, 184001 (2014).

[53] L. Li, S. Fang Lim, A. A. Puretzky, R. Riehn, and H. D. Hallen, Near-field enhanced ultraviolet resonance Raman spectroscopy using aluminum bow-tie nano-antenna, Appl. Phys. Lett. **101**, 113116 (2012).

[54] T. D. Dao, C. V. Hoang, N. Nishio, N. Yamamoto, A. Ohi, T. Nabatame, M. Aono, and T. Nagao, Dark-field scattering and local SERS mapping from plasmonic aluminum bowtie antenna array, Micromachines **10**, 468 (2019).

[55] B. Wang, S. C. Singh, H. Lu, and C. Guo, Design of aluminum bowtie nanoantenna array with geometrical control to tune LSPR from UV to near-IR for optical sensing, Plasmonics **15**, 609 (2020).

[56] H. Fischer and O. J. F. Martin, Engineering the optical response of plasmonic nanoantennas, Opt. Express **16**, 9144 (2008).

[57] A. Mohammadi, V. Sandoghdar, and M. Agio, Gold, copper, silver and aluminum nanoantennas to enhance spontaneous emission, J. Comput. Theor. Nanosci. **6**, 2024 (2009).

[58] G. H. Chan, J. Zhao, G. C. Schatz, and R. P. Van Duyne, Localized surface plasmon resonance spectroscopy of triangular aluminum nanoparticles, J. Phys. Chem. C **112**, 13958 (2008).